J. Fluid Mech. (1989), *vol.* 204, *pp.* 359–387
Printed in Great Britain

Structure of the turbulent flow field under breaking waves in the surf zone

By KAZUO NADAOKA, MIKIO HINO AND YOSHIJI KOYANO

Tokyo Institute of Technology, 2-12-1, O-okayama, Meguro-ku, Tokyo 152, Japan

(Received 10 February 1987 and in revised form 18 July 1988)

The structure of turbulence and its role in the breaking wave dynamics within the surf zone have been investigated through laboratory experiments using several flow visualization techniques and a fibre-optic LDV system. The results indicate that there exists a characteristic structure of large-scale eddies referred to here as 'horizontal eddies' and 'obliquely descending eddies', which has a significant role in the generation of Reynolds stress and thus affects the deformation of the mean flow field. The experiments also reveal that these eddies caused by the wave breaking bring a large amount of vorticity (with non-zero average) into otherwise almost irrotational velocity fields, resulting in the generation of vorticity-related mean flow fields as well as turbulence (vorticity-containing velocity fluctuation). This means that the breaking waves in the surf zone can be regarded as *pseudowaves* which consist of irrotational velocity components as 'wave motion' and appreciable amounts of rotational mean velocity components as 'eddying motion' (with non-zero mean vorticity) together with turbulence. It is found that the generation of the mean rotational velocity component due to wave breaking causes considerable increase in mass and momentum transport, as compared with ordinary non-breaking waves, and thus a decrease in wave height.

1. Introduction

As waves propagate through a shoaling region, they eventually break, resulting in intensive turbulence within the underlying flow field. Turbulence is one of the most significant phenomena in nearshore wave dynamics, because it may fundamentally characterize the flow field of the breaking wave region, and thus is closely related with phenomena such as wave damping, sediment transport, and thermal diffusion. Hence investigation of the turbulence under breaking waves is crucial for comprehensive understanding of wave dynamics in the nearshore zone. Unfortunately, any deductive analysis based on a definite basic equation is not possible for breaking waves because of the complexity of the turbulence phenomena themselves. Therefore, we must adopt alternative somewhat inductive or heuristic approaches based on field or laboratory experiments to analyse the turbulence flow field structure under breaking waves.

Until recently, knowledge of the turbulence structure has been quite limited, mainly because of the difficulty of velocity measurements. Thus, the analysis and estimation of breaking waves have almost entirely depended on some empirical methods. Recent experimental studies using new velocimeters, such as a laser-Doppler velocimeter or a hot-film anemometer with a split-type sensor have given some insight into the turbulent velocity field within the surf zone, as indicated by

Stive (1980), Stive & Wind (1982), Nadaoka & Kondoh (1982), Sakai, Inada & Sandanbata (1982), Sakai, Sandanbata & Uchida (1984), Hattori & Aono (1985) and others. However, understanding of the turbulent velocity field in the surf zone is still incomplete.

Recent developments in experimental research on turbulence using a flow visualization technique and based on the conditional-sampling concept have revealed that a turbulent flow field is essentially characterized by a coherent turbulence structure with large-scale eddies which depends on the flow geometry concerned. A careful observation of the velocity field within the surf zone indicates that one of the outstanding features of the velocity field under breaking waves is the generation of large-scale vortices associated with the breaking of the water surface at the front face of the waves. From the results of flow visualizations, Peregrine & Svendsen (1978) suggested the resemblance of the flow structure under turbulent bores to that of the usual turbulent mixing layer in the toe region of the bore and to a wake in the downstream decay region. Battjes & Sakai (1981) also pointed out, from their experiments on a steady breaker generated in a unidirectional flow with a submerged hydrofoil, that the turbulent flow structure is similar to that of a plane wake. However, it is still open to discussion whether such simple analogies are valid for breaking waves, because in both cases properties such as wave motion are not taken explicitly into account in their arguments on the velocity field structure.

In the present paper, an attempt to clarify the flow structure, mainly through investigating the intrinsic characteristics of the large-scale eddies under breaking waves by means of several flow visualization techniques and Eulerian velocity measurements, will be made. The results of the experiments will show that, under the breaking waves in the surf zone, there exist characteristic structures of the large-scale eddies, referred to here as 'horizontal eddies' and 'obliquely descending eddies'. The experiments also reveal that these eddies bring a large amount of vorticity with non-zero average into otherwise almost irrotational velocity fields, resulting in vorticity-related mean flow fields as well as turbulence as vorticity-containing velocity fluctuations. This means that breaking waves in the surf zone can be regarded as *pseudowaves* which consist not only of an irrotational velocity component as 'wave motion', but also of appreciable amounts of rotational velocity components as 'eddying motion' with non-zero mean vorticity. Dividing a measured mean velocity field into these two components by using the separation method proposed, we shall find that the mean rotational velocity component generated through the wave breaking process has an essential role in the breaking wave dynamics in the surf zone; i.e. the generation of the mean rotational velocity component results in a considerable increase in mass and and momentum fluxes as compared with ordinary waves. Furthermore, by inversely estimating a water surface profile corresponding to the separated irrotational velocity field, we shall find that the vorticity effects have a fundamental influence also on the dynamics governing the water surface elevation of breaking waves.

2. Experimental set-up and procedure

2.1. *Experimental apparatus*

The wave channel used for the experiments is 0.6 m deep, 0.4 m wide and 20 m long, equipped with a flap-type wave generator. A model beach with fixed bed, which consists of a horizontal section of 3.6 m in length and a slope of 1 on 20 in front, is installed at one end of the channel as shown in figure 1. The still water depth at the

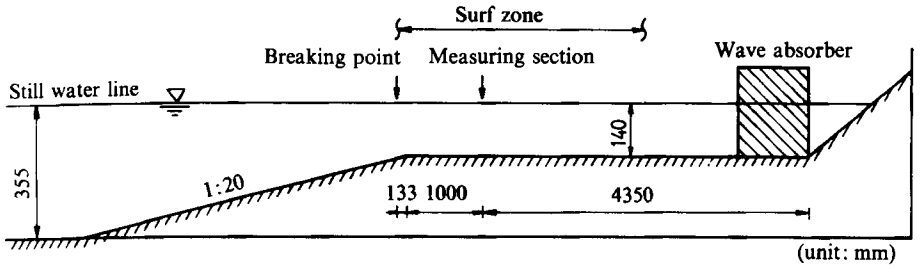

FIGURE 1. Experimental equipment.

shelf section is kept at 14 cm throughout the experiments. A wave absorber is mounted at the beach end to diminish wave reflection.

2.2. *Procedure for experiments*

The experiment was carried out under the conditions of wave period $T = 1.36$ s, equivalent offshore wave height $H_0' = 11.6$ cm, and offshore wave steepness $H_0'/L_0 = 0.0405$. Regular waves generated by the wave maker produced a spilling-type breaker just outside the shelf section. The depth and wave height of the breaker, h_b and H_b, are 14.7 cm and 14.9 cm, respectively. Velocity measurements were carried out at a location 113 cm shoreward from the breaking point, as shown in figure 1. At the measuring section, where the wave set-up was 0.82 cm, breaking waves were confirmed to be well developed into a so-called 'turbulent bore', and simultaneous measurements of the horizontal and vertical velocities were made at 11 elevations.

2.3. *Data acquisition and reduction*

Velocity measurements were carried out with a two-component fibre-optic laser-Doppler velocimeter of backscattered fringe mode (FLV) which has been recently developed by Hino *et al.* (1984) at Tokyo Institute of Technology and Nihon Kagakukogyo Co. Ltd. The velocimeter can measure horizontal and vertical velocity components, u and w, simultaneously with two-colour laser beams, He–Ne of 15 mW and Ar of 20 mW. The FLV has an L-shaped probe whose stem is 1.2 cm in diameter and 20 cm in length. The focus of a front lens mounted at the tip of the probe is sufficiently short, 1.7 cm, that the FLV is not as much affected by entrained air bubbles as a usual LDV system. Hence the FLV has the advantage that it is applicable even to the region above the trough level of waves, where the entrained air bubbles attain relatively high concentration levels, though the accuracy of measurement may decrease somewhat because of drop-out of the signal due to air bubbles. To improve the S/N ratio of Doppler signals, a small amount of poster colour paint, of particle diameter of order 1 μm, was seeded in the wave tank as scattering particles. Two frequency shifters with Brag-cell optical units were used to allow velocity measurements for oscillatory flows. The Doppler signals were processed with two frequency tracker-type signal-processing electronic units, which work the track-and-hold operation when signal drop-out occurs. The water surface elevation η was measured with a capacitance-type wave gauge at a location directly above the velocity measuring points.

The velocity and water surface elevation data were taken simultaneously and recorded as digitized data at an interval of 0.01 s into a transient memory (WFRA-no 8700 series; Kikusui Electronics Co.). Then the data were transmitted through a desk-top-type computer, HP9835, to magnetic tapes for the subsequent data

analysis. The time series of u, w and η were divided into individual data sets, $\{u_i, w_i, \eta_i\}$ $(i = 1, 2, \ldots, I)$, by applying the zero-up crossing method to η. The number of adopted data sets, I, was about 45. Ensemble-averaged data, $\langle u \rangle$, $\langle w \rangle$ and $\langle \eta \rangle$, were obtained by calculating phase averages of $\{u_i, w_i, \eta_i\}$, the definition of which will be given later in equation (1).

2.4. *Flow visualization*

To grasp the Lagrangian characteristics of the water particle movements, some observations were carried out by means of several flow visualization techniques. One of the simplest ways to achieve the visualization is to regard a number of air bubbles entrained through the wave breaking process as tracers for the visualization. Although the trajectories of the air bubbles are not exactly the same as those of the water particles owing to the buoyancy effect, the discrepancy is not so significant because the rising velocity in still water is smaller than 0.1 cm/s for tiny air bubbles of the order 0.1 mm or less in diameter. Some artificial beads with nearly neutral buoyancy were also utilized as tracers for the visualization. Detailed descriptions of them will be left for the subsequent sections.

3. Flow visualization of large-eddy structure

3.1. *Overall flow structure visualized by entrained air bubbles*

Figure 2 shows instantaneous contour lines of breaking water surface elevation in the region of the velocity measuring section. The contours were delineated with a set of stereoscopic photos for a plan view of the water surface which was made discernible by mixing a small quantity of poster colour paint in the water. It is found from this figure that, near the front edge of the bore, the overall features of the water surface undulation indicate the existence of a nearly two-dimensional flow structure parallel to the wave crest, although the two-dimensionality is not so obvious owing to the presence of some irregularities of the water surface configuration.

Figure 3 shows a plan view 9.0 cm above the bottom of the flow structure with entrained air bubbles. The photo was taken in the dark by projecting a horizontal slotted light into the water. The brighter regions in the photo, which correspond to the air bubble regions 20–50 cm behind the wave crest, show a spot-like feature, indicating the development of strong three-dimensionality of the flow structure behind the wave crest.

Figure 4 is an example of a side view around the measuring section. The size of the mesh shown in the photo is 10 cm × 7 cm. The photo is a frame copied from a movie film taken by a 16 mm cinecamera with a shutter speed of 1/136 s, and shows clearly the tortuous configuration of the entrained air bubble region around the wave crest. This feature corresponds to the two-dimensional flow structure mentioned above. In a moving frame of reference, on the other hand, the flow field exhibits a closed pattern of streamlines, as shown in figure 5. Further, as will be shown later in figure 19, the flow field in this region has appreciable vorticity. Hence the tortuous nature of the air bubble region shown in figure 4 can be considered as the appearance of a large-scale eddy structure having a horizontal axis parallel to the wave crest. This type of eddy structure has also been observed in the experiments by Miller (1976), Peregrine & Svendsen (1978), Nadaoka & Kondoh (1982), Peregrine (1983) and others, and will be referred to here as 'horizontal eddies'.

Figure 6 is a sequence of pictures traced from the 16 mm movie film taken in a fixed frame of reference. The time interval between adjacent figures is 1/32 s. The air

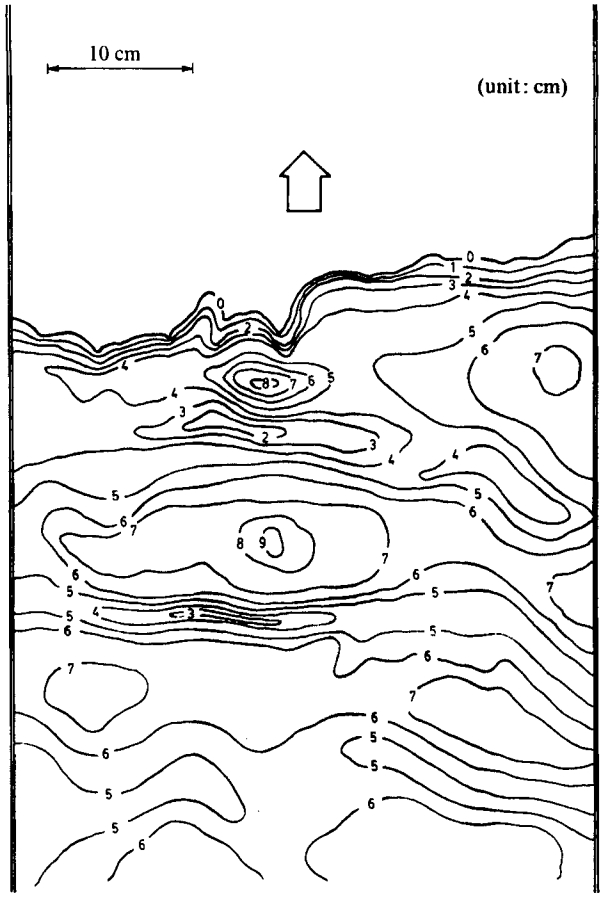

FIGURE 2. Contour lines of instantaneous water surface elevation around the wave crest.

bubble region is the area partly enclosed by a solid line in which a number of tiny segments indicate the direction of particle movement, though their length does not accurately correspond to their magnitude of velocity. This figure shows that the configuration of the lower edge of the air bubble region evolves into obliquely downward projected shapes with the propagation of the waves. Close examination of figures 5 and 6 shows that the protruding air bubble region extends obliquely downwards on a stretched flow field around the saddle point between the two adjacent horizontal eddies, as depicted schematically in figure 7. Accordingly, the initial downward development of the flow structure can be considered to be closely related to the stretched flow field due to the horizontal eddies.

Figure 8 is another example showing side views in the region of the velocity measuring section, and is a sequence of pictures taken successively by a motor-driven 35 mm camera. The portion indicated by the arrow shows the evolution of the lower edge of the entrained air bubble region which is stretched in an inclined direction to the propagation of the bore. At stage (*d*), the stretched portion almost reaches the bottom. This is consistent with the fact revealed by Nadaoka & Kondoh (1982) that the intensity of turbulence at the bottom shows a close correlation with that of the upper-layer turbulence. Visual observations have shown that the air bubbles in the inclined stretched portions exhibit vortical motion with an axis of rotation along

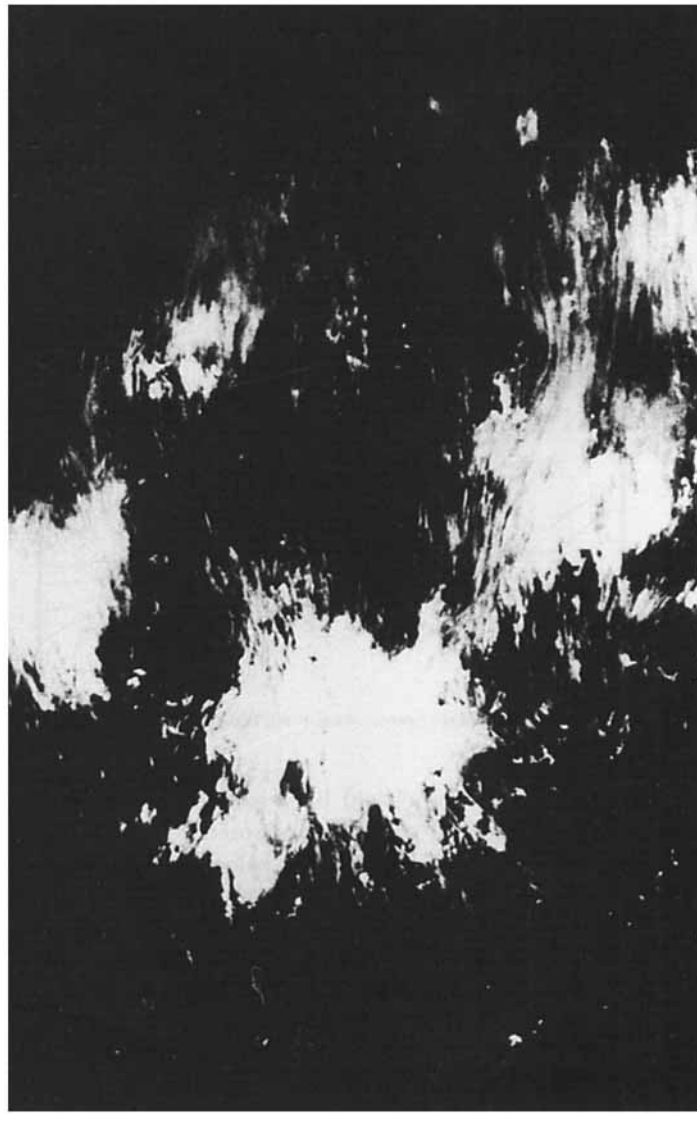

FIGURE 3. A plan view at 9 cm above the bottom behind the wave crest, which was taken in the dark under illumination from a horizontal light plane.

the direction of the stretch. Hence such inclined vortical fluid motion involving the air bubbles is considered to be responsible for the appearance of the spotty feature in figure 3. The inclined eddy structure will be referred to here as 'obliquely descending eddies'.

In figure 3, we can also see that the air-containing spots appear irregularly in

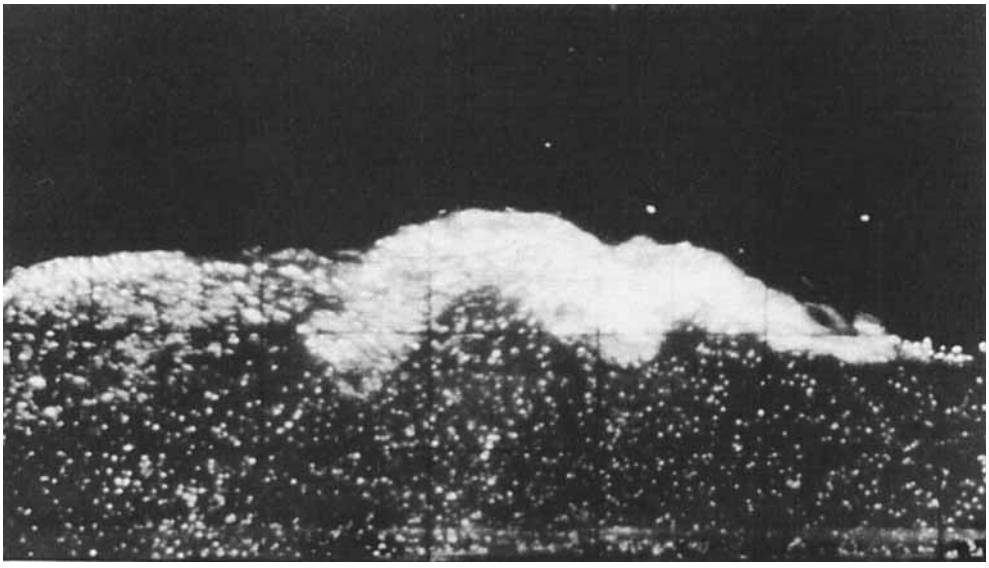

FIGURE 4. A side view around the velocity measuring section (taken from a 16 mm movie film).

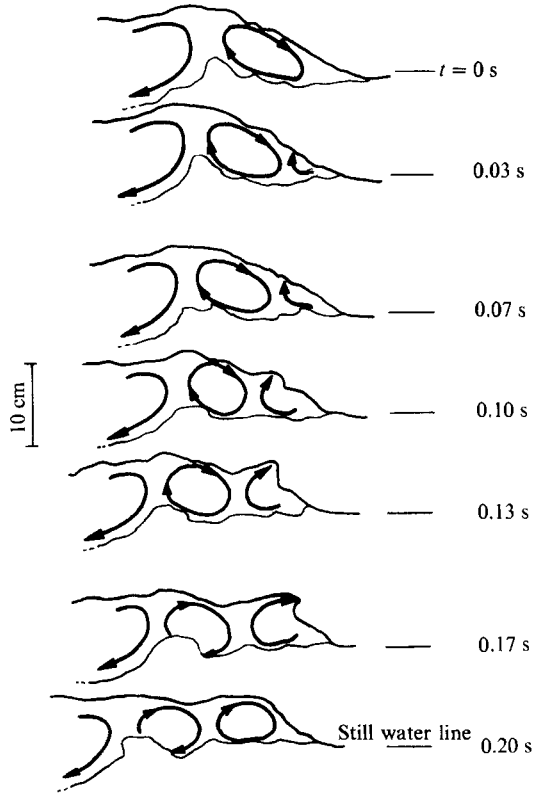

FIGURE 5. Evolution of entrained air bubble region and the pattern of the related streamlines (moving frame).

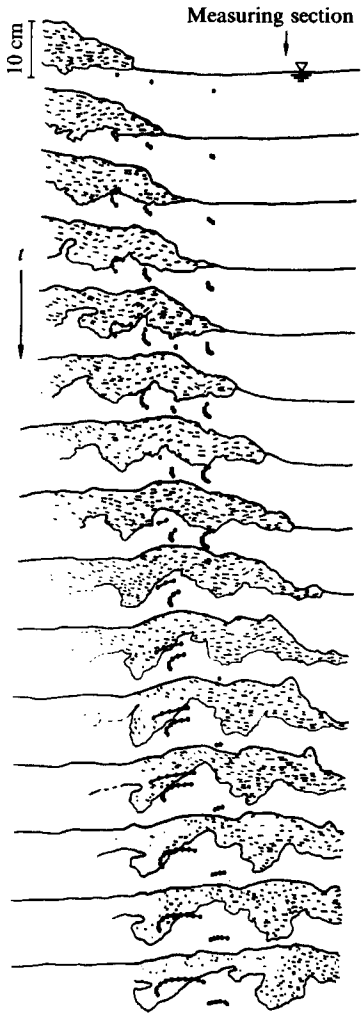

FIGURE 6. Evolution of entrained air bubble region and movements of neutral density particles (fixed frame).

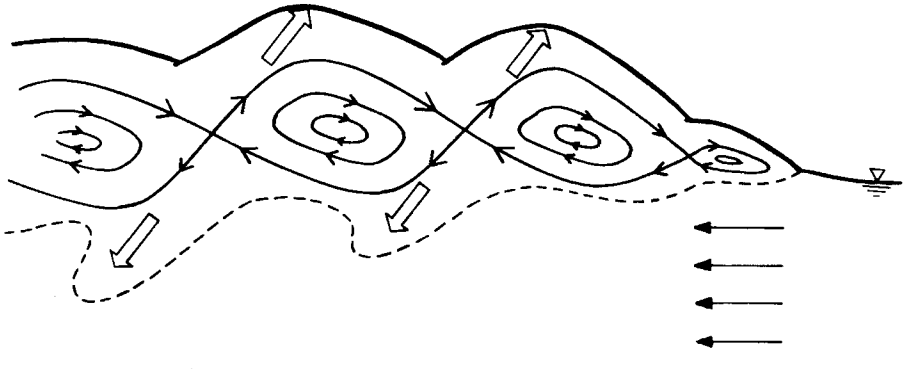

FIGURE 7. Relation between stretched flow field around saddle points of streamlines and evolution of the oblique eddies.

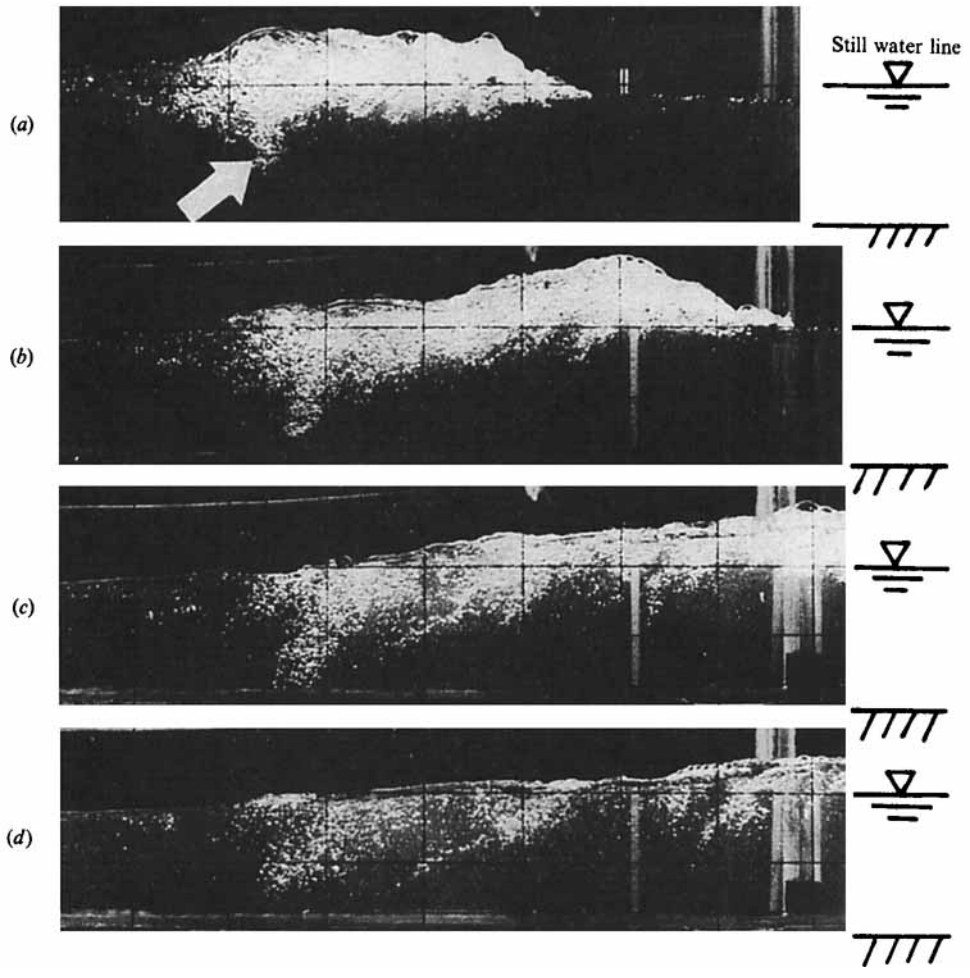

FIGURE 8. A sequence of pictures of side views around the velocity measuring section taken successively by a motor-driven 35 mm camera.

space. This suggests that the regulation effect by the sidewalls on the oblique eddies is not very significant. Further, it was confirmed that variation of the spacing between the sidewalls yields no appreciable change in the overall features of the eddy structure, although the development of the oblique eddies near the walls is slightly enhanced by their presence. Hence, no essential role seems to be played by the sidewalls in the generation of the obliquely descending eddies.

Generally speaking, the eddies that are more effective than most of the others in extracting energy from the mean flow are vortices whose principal axis is not perpendicular to the mean flow, but roughly aligned to that of the mean strain rate (see e.g. Tennekes & Lumley 1972, p. 41). As will be shown later in figure 18, the principal axes of the mean strain rate of the phase-averaged velocity field around and behind the wave crest are in a plane perpendicular to the crest line and are mostly tilted at angles of about 45° or less to the horizontal, which almost coincides with the direction of stretch of the oblique eddies. Furthermore, the principal strain rate shows relatively large values in those regions. Hence, such deformation characteristics of the mean flow field are responsible for the development of the oblique

FIGURE 9. A photo taken from an observatory pier at the Ajigaura coast facing the Pacific Ocean, which shows a plane view of a bore propagating from left to right.

eddies. We can expect, furthermore, that the evolution process of the eddies may be also influenced by the buoyancy effect due to air bubbles involved in the eddies, although discussions on this problem are to be left for future studies. Therefore, the quick deformation from the nearly two-dimensional structure at the wave front to the obliquely eddying structure behind the wave crest may be considered as an inherent process in breaking waves.

Such a deformation process can be also confirmed, for example, by a field observation of breaking waves within the surf zone. A bird's-eye view, shown in figure 9, which was taken at an observatory pier located on the Ajigaura coast facing the Pacific Ocean, shows a bore propagating from left to right. It can be clearly seen in this photo that there exists a ruffled fringe along the crest line at the wave crest, while some entrained air bubble spots appear behind it. This is quite similar to the above-mentioned feature of the overall flow structure for the present experiments.

In summary, the large-scale eddy structure of breaking waves in the surf zone can be depicted as follows. Around the wave crest, dominant eddies have a rather two-dimensional flow structure, the axis of which is parallel to the crest line (horizontal eddies), while behind the wave crest, the flow structure develops quickly into that with strong three-dimensionality, i.e. eddies stretched obliquely downwards (obliquely descending eddies). Figure 10 shows a schematical representation of the eddy structure of breaking waves.

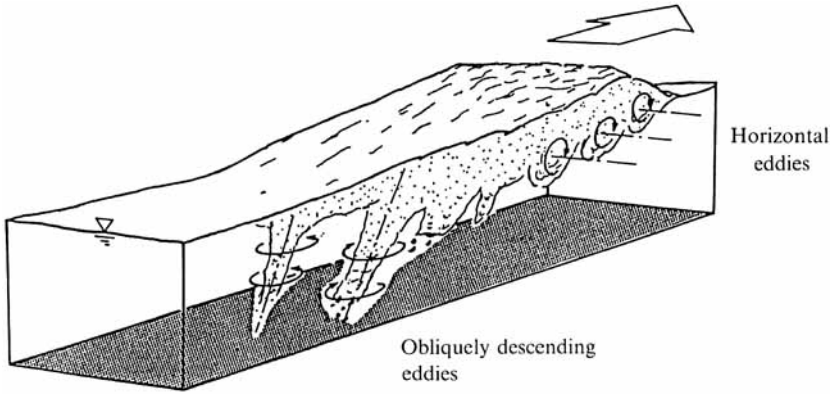

FIGURE 10. Schematic representation of the large-scale eddy structure under breaking waves.

3.2. *Lagrangian characteristics of the water particle movements*

Several flow visualizations using particle tracing techniques were carried out to investigate the Lagrangian behaviour of the water particles. A number of scattered speckles under the air bubble regions, shown in figure 4, are almost neutrally buoyant polystyrene beads with a diameter of about 1 mm. The time evolution of the trajectories of the particle movements under the entrained air bubble region is represented in figure 6 as the growth of traces of the particles. From this figure, it is seen that the tracers under the air bubble region show regular orbital motion. Hence the flow structure beneath the air bubble region around the wave crest is considered to be that of a potential flow field, though the water particle movements behind the wave crest are occasionally affected by the obliquely descending eddies, as described below.

To visualize the particle movements in the air bubble regions, the technique mentioned above is not applicable because it is quite difficult to distinguish the tracers from the air bubbles. So, polypropylene beads, 3 mm in diameter and painted with fluorescent dye, were used as tracers for the visualization under lighting by ultraviolet lamps. As the specific gravity of the polypropylene beads is 0.90, a small amount of aluminium powder was tagged on the surface of the beads to obtain neutral buoyancy.

Examples of the trajectories of the tracers are shown in figure 11 (*a*, *b*) with the wave profiles at the inception of the particle tracing. The numbers on the trajectories represent the elapsed time shown in the table in each figure. In figure 11 (*a*), the trajectory near the water surface shows shoreward movement with relatively high speed. This corresponds to the particle behaviour within the horizontal eddies. The particle movements at middepth of the water represents the combined effects due to orbital motion and the offshoreward mean flow (or so-called 'undertow'). On the other hand, the tracers in figure 11 (*b*) show rather irregularly descending movements. These correspond to the particle movement when the particles are involved in the obliquely descending eddies. In this case, the particles almost reach the bottom (cf. figure 8). This suggests a possible mechanism by which bottom sediment is set into suspension; that is, the sediment may be lifted up from the bottom by the attack of the obliquely descending eddies.

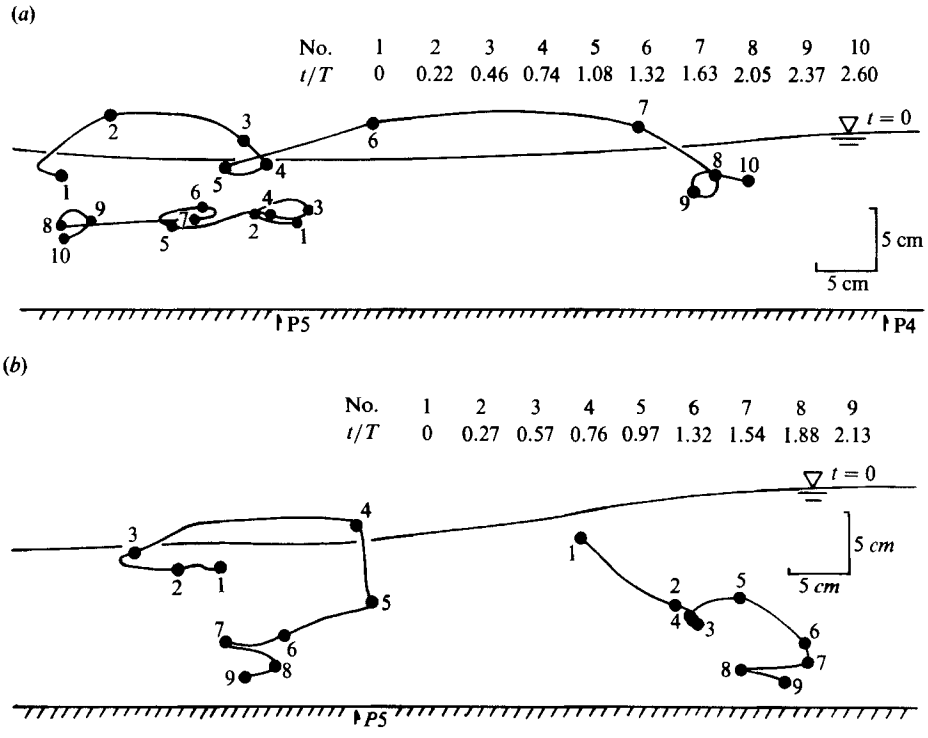

FIGURE 11. Trajectories of neutral-density particles.

3.3. *Reynolds stress generated by the large-scale eddies*

In figure 4, the air bubbles show finite streak-like segments, whereas the artificially introduced beads appear as dots rather than streaks below the air bubble region. This means that the water particles in the upper region move considerably faster than those in the lower region. Moreover, as shown in figure 6, high-horizontal-speed fluid protrudes sporadically into the lower region, as the eddy structure evolves into the obliquely descending eddies.

The descending movement of the water particles in the upper region, whose horizontal velocity component is considerably larger than that in the lower region, as already mentioned, is expected to contribute to the generation of Reynolds stress at the interface between the upper and lower regions. To confirm this point, a close examination was carried out of the velocity records obtained with the FLV at 11.5 cm above the bottom, where the interface under the wave crest is located. Figure 12 shows records of instantaneous Reynolds stress $-uw$ and of η, u and w. Successive video images of the side view of the channel, which represent the time evolution of the eddy structure, were also taken simultaneously with the velocity measurements. The simultaneity was ensured by recording a video image of a time mark corresponding to the start time of the velocity measurement. The arrows shown at the bottom of the figure indicate the instants when the large-scale eddy travels down through the velocity measuring point. In this figure, the instants when the instantaneous Reynolds stress $-uw$ shows remarkably large values almost coincide with those indicated by the arrows. This means that the downward movements of the large-scale eddies with high-horizontal-speed fluid make a significant contribution to the generation of the Reynolds stress.

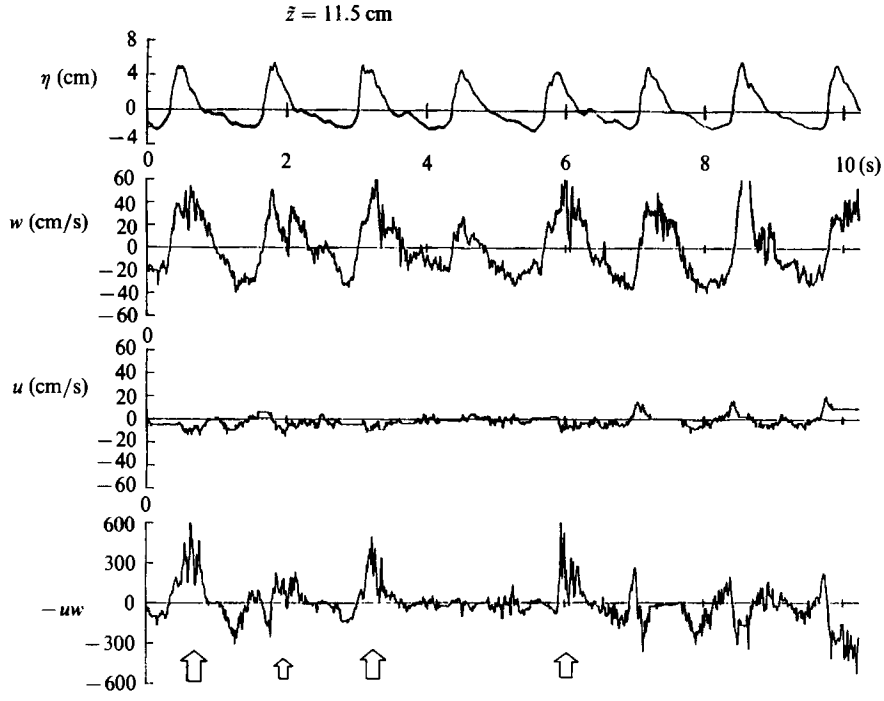

FIGURE 12. Records of instantaneous Reynolds stress $-uw$ with those of η, u and w. The arrows indicate the instants when the large-scale eddy goes down through the velocity measuring point.

4. Phase-averaged flow field structure

As already mentioned, the large-scale eddies play an essential role in the dynamic turbulent process of the velocity field under the breaking waves. In the present section, this role will be examined through some phase-averaged properties of the flow field.

4.1. *Phase-averaged velocity field* $\langle \boldsymbol{u} \rangle$

In usual steady turbulent flows, time averages of a velocity record may be substituted for an ensemble-averaged velocity, by assuming an ergodic property of the probabilistic structure of the velocity field. However, such ergodicity cannot hold for the flow field concerned here, because the presence of orbital wave motion may produce a probabilistic non-stationarity. For this reason, in the present study the ensemble-averaged velocity $\bar{\boldsymbol{u}}$ is obtained approximately by calculating a phase-averaged velocity $\langle \boldsymbol{u} \rangle$ defined as

$$\langle \boldsymbol{u}(\boldsymbol{x}, \omega t) \rangle = \frac{1}{I} \sum_{i=0}^{I-1} \boldsymbol{u}(\boldsymbol{x}, \omega(t + iT)), \tag{1}$$

where $\boldsymbol{u}$ is a velocity vector, $\langle \cdot \rangle$ an operator to take a phase average, I a sample number, T a wave period, ω an angular frequency, $\boldsymbol{x}$ a position vector and t time.

Figure 13 shows the phase-averaged velocity vector $\langle \boldsymbol{u} \rangle$ for which the sample number I is about 45. The symbol $\tilde{z}$ in the figure represents the vertical coordinate measured upward from the bottom. The figure shows that the shoreward velocity around the wave crest increases its magnitude with height except for the region close to the bottom, whereas the offshoreward velocity around the wave trough *decreases* with height. As will be shown later in detail, this is due to the effects of vorticity

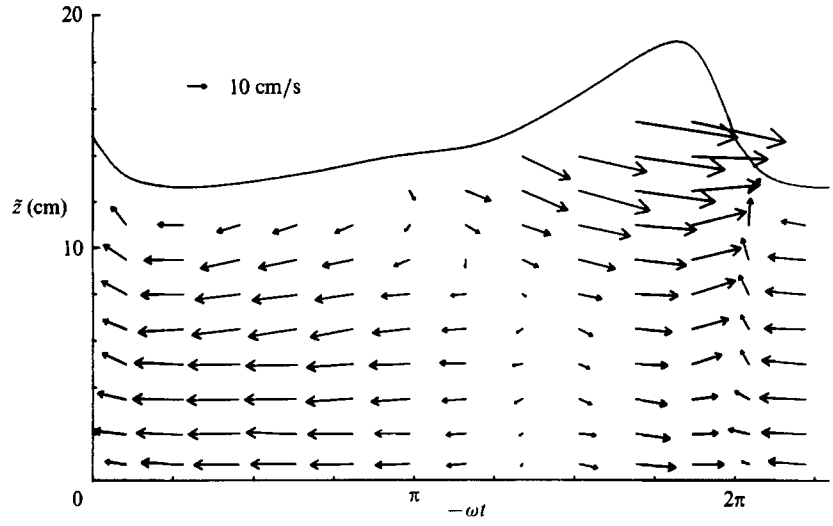

FIGURE 13. Phase-averaged velocity vector, $\langle \boldsymbol{u} \rangle$.

associated with the large-scale eddies generated during the wave breaking process. The bottom-originated vorticity also affects the vertical velocity profiles near the bottom, although the effects are not as significant as that due to the eddies in the upper region because the bottom roughness is negligibly small in this case.

4.2. *Turbulence intensity*

Usually in discussions on turbulence, we consider a velocity field $\boldsymbol{u}$ by dividing it into an ensemble-averaged component $\bar{\boldsymbol{u}}$ and an irregularly fluctuating component $\mathbf{u}'$, and define the turbulence by the latter component, i.e.

$$\boldsymbol{u} = \bar{\boldsymbol{u}} + \boldsymbol{u}'. \tag{2}$$

In the present situation, however, such a simple definition of turbulence is not valid because the irregularity of velocity fluctuations is not a sufficient condition for the definition of the turbulence. For example, we cannot regard irregular velocity fluctuation under random waves as turbulence.

Another essential property of turbulence is its *rotationality*. That is, we should consider $\boldsymbol{u}$ by dividing it also into irrotational and rotational velocity components, $\boldsymbol{u}_{\mathrm{p}}$ and $\boldsymbol{u}_{\mathrm{e}}$. Then we can describe $\boldsymbol{u}$ as

$$\boldsymbol{u} = \bar{\boldsymbol{u}}_{\mathrm{p}} + \bar{\boldsymbol{u}}_{\mathrm{e}} + \boldsymbol{u}'_{\mathrm{p}} + \boldsymbol{u}'_{\mathrm{e}}. \tag{3}$$

Among these components, turbulence should be defined by $\boldsymbol{u}'_{\mathrm{e}}$, the vorticity-containing irregular velocity component. However, it is a formidable task to extract $\boldsymbol{u}'_{\mathrm{e}}$ with sufficient accuracy from the velocity data.

The phase-average method, one of the conventional methods for detecting turbulence under breaking waves, defines the turbulence as the difference of instantaneous velocity fluctuation from the phase-averaged velocity defined in (1). This method cannot get rid of the irrotational velocity fluctuation $\boldsymbol{u}'_{\mathrm{p}}$ which arises even when the breaking waves are generated with the periodic paddle motion of a wave maker. This is because the inception of breaking of incident waves and their subsequent development into a turbulent bore have a non-deterministic element which is sensitive to any irregularities inherent in the breaking wave field, and hence

the time history of the water surface elevation itself varies considerably from wave to wave.

Hence, for the turbulence detection in the present study, we have used a numerical filtering method, which is another conventional method for surf zone turbulence, and defines the turbulence as output signals from a numerical filter, though the method also has the disadvantage that it is difficult to definitely determine the cut-off frequency or the moving average time, because the spectral velocity components as 'waves' and 'turbulence' are mutually superimposed in a range of the frequency domain. The moving average time in the present case was selected as 0.1 s, which corresponds to the cut-off frequency of 5 Hz, by taking into account the results of a spectral analysis of velocity fluctuations which shows that an appreciable amount of the energy spectral components of the higher harmonics to the fourth or fifth order of wave motion is included in the records of the water surface and the velocity fluctuation.

Figure 14 (*a*, *b*) shows the distribution of horizontal and vertical components of the turbulence intensity, u' and w', respectively. In the calculation of these quantities, the velocity data during signal drop-out due to air bubbles were removed. It is found from these figures that both u' and w' have their peak at the lower edge of the eddy region, where the shear and the strain rate of the flow field have very large values, as will be shown later, though the contour lines for u' have a longer tail toward the wave trough than those for w'.

4.3. *Reynolds stress*

Reynolds stress has been detected by the two methods, i.e. the moving average method and the phase-average method. By the former method, the Reynolds stress was calculated as $-\langle u'w'\rangle$, where u' and w' are the turbulent components obtained by the numerical filtering method mentioned above. While, by the phase-average method, the Reynolds stress was calculated as $-\langle (u-\langle u\rangle)(w-\langle w\rangle)\rangle$, which can be considered nearly equal to $-\langle u'_{\mathrm{e}} w'_{\mathrm{e}}\rangle$ under the assumption that the occurrence of $\boldsymbol{u}'_{\mathrm{p}}$ is independent of the primal incident waves. Figures 15 and 16 show the results obtained by these two methods. In both the cases, the Reynolds stress distribution shows its peak value at the lower edge of the eddy region under the wave trough. This is consistent with the description in §3.3; i.e. the intensive magnitude of the instantaneous Reynolds stress is produced by the downward movements of high-horizontal-speed fluid within the eddy region in the evolution process of the large-scale structure from the horizontal eddies to the obliquely descending eddies.

The magnitude of the peak value by the phase-average method is two orders larger than that by the moving average method. This is considered to be due to the fact that the moving average method may not completely detect the Reynolds stress due to the large-scale eddies. Conversely, this fact suggests that the Reynolds stress is produced mainly by the large-scale eddies.

4.4. *Phase-averaged deformation rate of the velocity field*

Since the breaking waves were confirmed to show no noticeable deformation of their shape through propagation over a distance of one wavelength around the measuring section, the horizontal axis $-\omega t$ in figure 13 may be regarded approximately as kx. Thus, by taking numerical differentiations of the phase-averaged velocity field $\langle \boldsymbol{u}\rangle$ as defined in (1), we can calculate quantities related to deformation of the velocity field $\langle \boldsymbol{u}\rangle$.

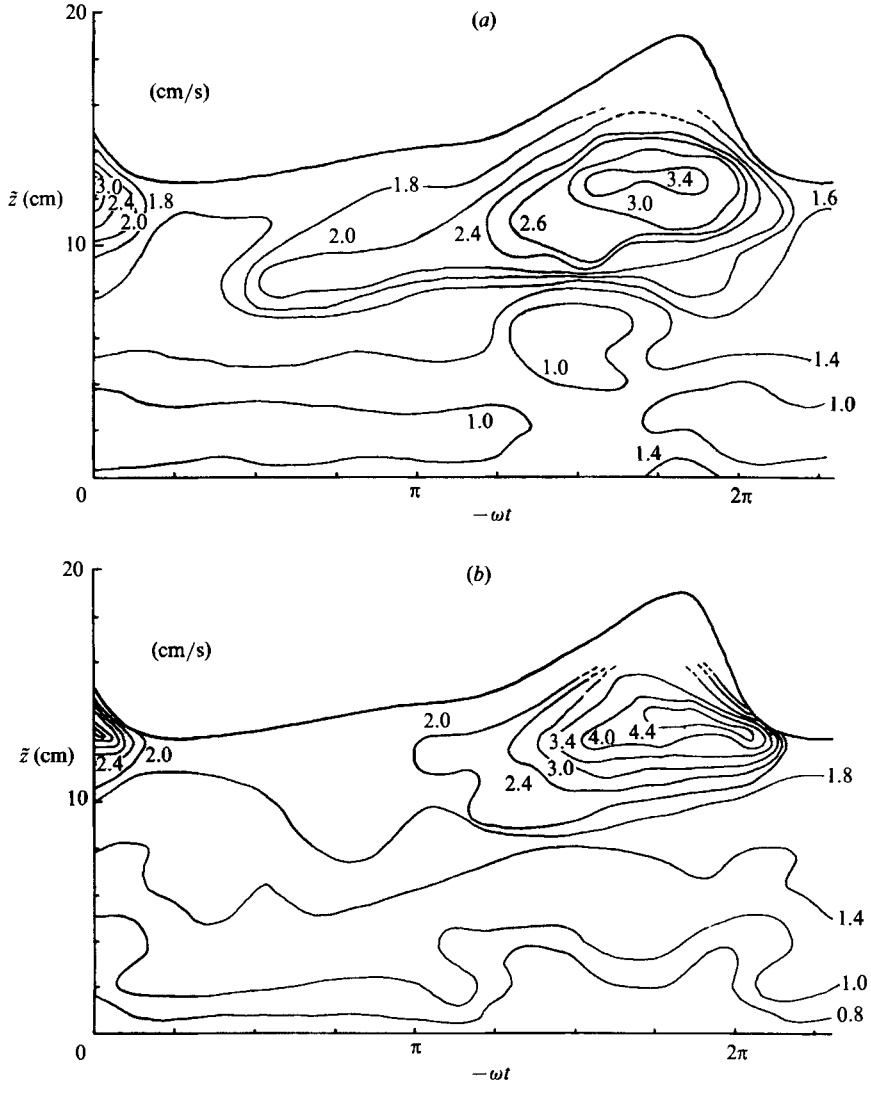

FIGURE 14. Distribution of horizontal and vertical components of turbulence intensity (*a*) u' and (*b*) w', detected by a moving average method.

4.4.1. *Shear-strain rate* $\langle \gamma_{xz} \rangle$

Figure 17 represents the phase-averaged strain rate $\langle \gamma_{xz} \rangle$ defined as

$$\langle \gamma_{xz} \rangle = \frac{\partial \langle w \rangle}{\partial x} + \frac{\partial \langle u \rangle}{\partial z}. \tag{4}$$

The figure shows that $\langle \gamma_{xz} \rangle$ has a peak value at the lower edge of the eddy region under the wave crest, similarly to the Reynolds stress shown above. This suggests that a usual eddy viscosity model for the Reynolds stress is applicable to such a velocity field.

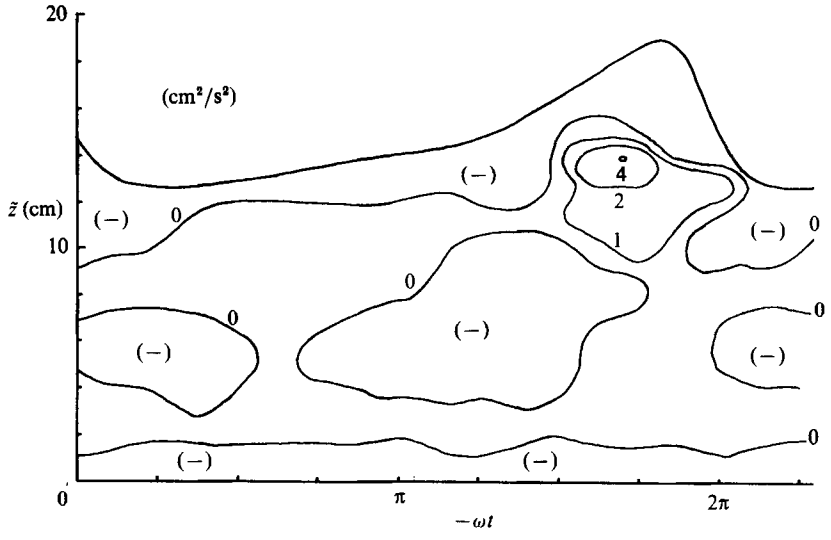

FIGURE 15. Reynolds stress detected by a moving average method.

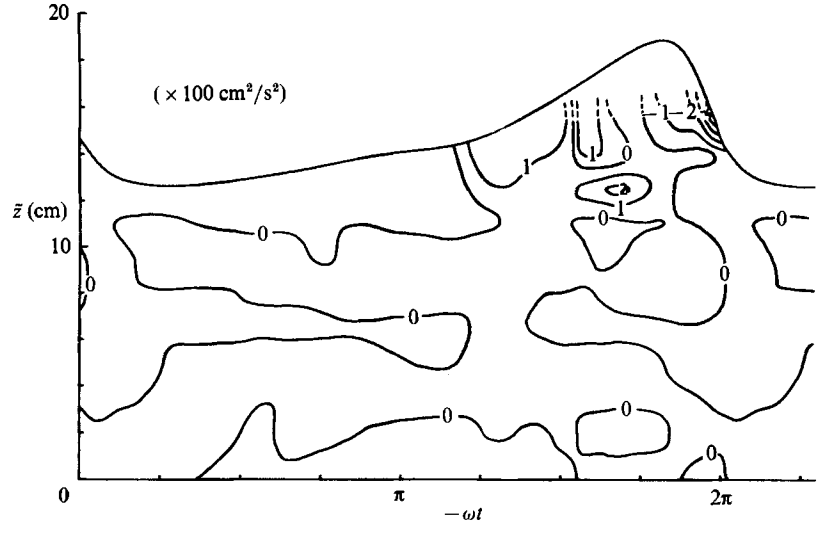

FIGURE 16. Reynolds stress detected by a phase-average method.

4.4.2. *Principal axes and strain rates*

The principal axes and strain rates are calculated from the eigenvectors and eigenvalues, respectively of the shear-strain tensor:

$$\begin{bmatrix} 2\dfrac{\partial\langle u\rangle}{\partial x} & \dfrac{\partial\langle w\rangle}{\partial x}+\dfrac{\partial\langle u\rangle}{\partial z} \\ \dfrac{\partial\langle w\rangle}{\partial x}+\dfrac{\partial\langle u\rangle}{\partial z} & 2\dfrac{\partial\langle w\rangle}{\partial z} \end{bmatrix}. \tag{5}$$

The results of the calculation are shown in figure 18. The principal direction of the stretch is represented by arrows whose lengths are proportional to the principal

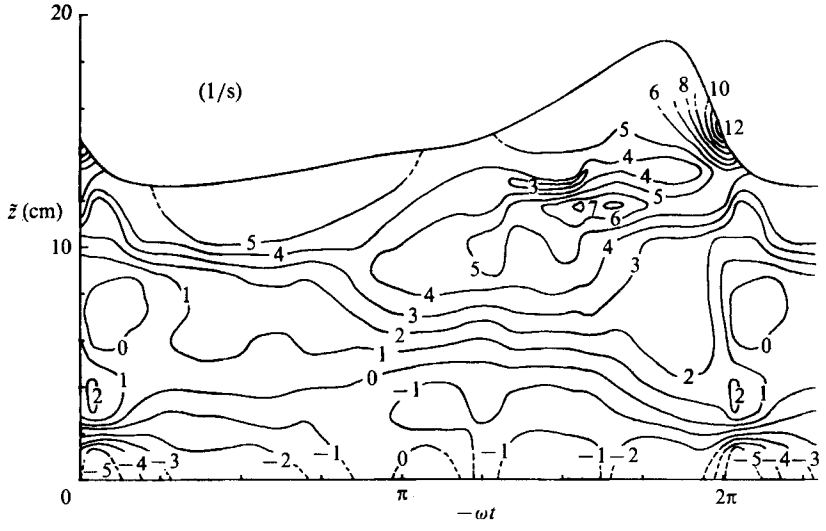

FIGURE 17. Phase-averaged shear-strain rate, $\langle \gamma_{xz} \rangle$.

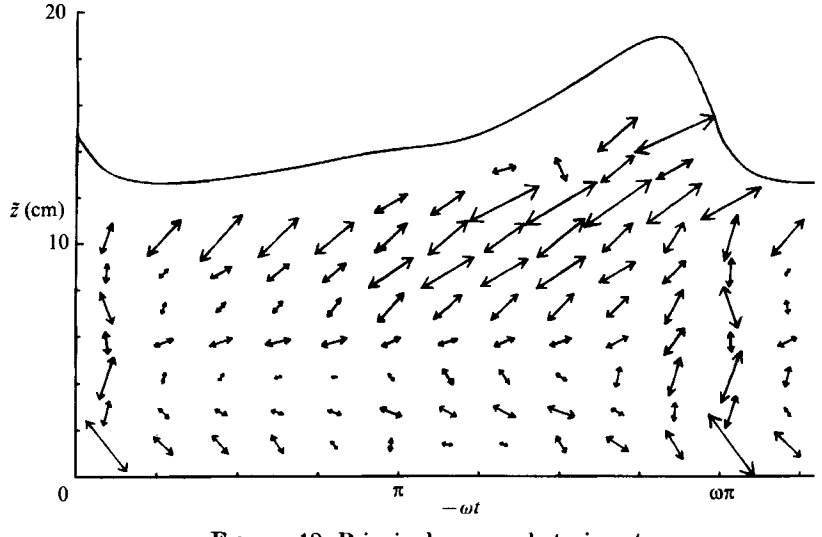

FIGURE 18. Principal axes and strain rates.

strain rates. From this figure, it is found that the flow field in the eddy region is stretched obliquely at a direction of about 45° or less to the horizontal. This direction almost coincides with that of the development and stretching of the obliquely descending eddies. This is closely related to the evolution of the oblique eddies, as already pointed out in §3.1.

4.4.3. *Vorticity* $\langle \zeta \rangle$

Figure 19 represents the phase-averaged vorticity calculated as

$$\langle \zeta \rangle = \frac{\partial \langle u \rangle}{\partial z} - \frac{\partial \langle w \rangle}{\partial x}. \tag{6}$$

The figure shows that there exists a marked peak of vorticity at the front face near

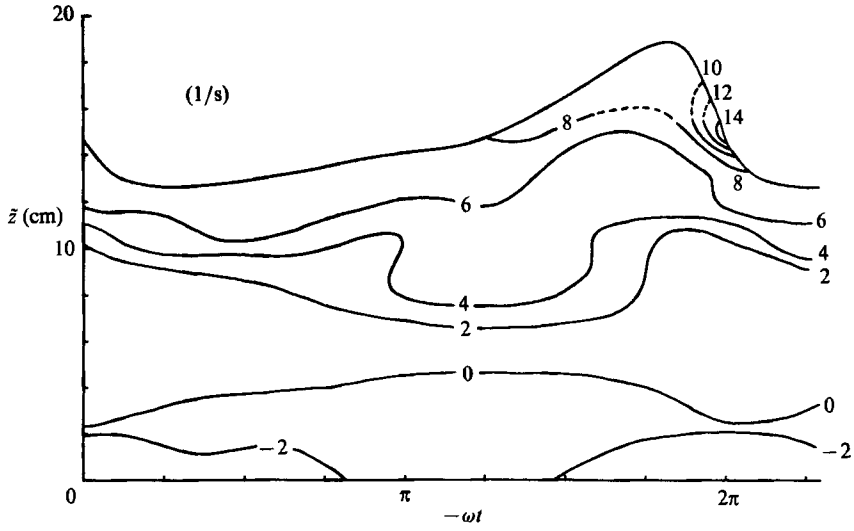

FIGURE 19. Phase-averaged vorticity, $\langle\zeta\rangle$.

the wave breaking and the vorticity decreases gradually towards the back and bottom of the wave. This means that the vorticity is generated at the front face by the wave breaking and is advected and diffused into the otherwise almost irrotational flow field. The bottom-originated vorticity is rather limited in magnitude and extent, because the bottom roughness is negligibly small in this case.

The generation of such a large amount of vorticity under breaking waves gives rise to some conspicuous effects on the velocity field and thus on the breaking wave dynamics, as will be seen in the next section.

5. Vorticity effects on the mean velocity field under breaking waves

As described above, breaking waves produce large-scale eddies with an appreciable amount of *mean* vorticity within the underlying flow field. This means that within the surf zone the ensemble-averaged velocity $\bar{\boldsymbol{u}}$ (or the phase-averaged velocity $\langle\boldsymbol{u}\rangle$) is composed not only of the irrotational component $\bar{\boldsymbol{u}}_{\mathrm{p}}$ (or $\langle\boldsymbol{u}_{\mathrm{p}}\rangle$) as wave motion but also of the rotational component $\bar{\boldsymbol{u}}_{\mathrm{e}}$ (or $\langle\boldsymbol{u}_{\mathrm{e}}\rangle$) as eddying motion (cf. (3)). From the original physical meanings, 'waves (irrotational)' and 'eddies (rotational)' are highly contrasting concepts. In the surf zone, however, the 'waves' coexist with a considerable amount of the 'eddies' with non-zero average, and this is one of the most significant characteristics of breaking waves. Therefore, a more comprehensive understanding of the velocity field structure within the surf zone may be achieved by revealing the effects of the mean vorticity associated with the large-scale eddies on the velocity field under breaking waves.

For the analysis of the vorticity effects, we need a method to separate a velocity field $\langle\boldsymbol{u}\rangle$ into irrotational and rotational components, $\langle\boldsymbol{u}_{\mathrm{p}}\rangle$ and $\langle\boldsymbol{u}_{\mathrm{e}}\rangle$. Unfortunately, all of the existing wave theories including Dean's (1965) stream function method, which was originally developed for non-breaking waves, cannot be used for this purpose because of the local breaking of the water surface.

Thus, an alternative method is proposed in the present paper by which the irrotational velocity component is calculated with a Fourier analysis of the velocity data at a point where the vorticity is substantially zero and thus the motion may be

assumed to be irrotational. The method will be outlined in what follows. Then the vorticity effects on the mass and momentum transport as well as on the water surface elevation will be examined through this velocity separation.

5.1. *Separation of rotational and irrotational velocity components*

According to the theory of vector analysis, a vector field under ordinary conditions may be separated into irrotational and solenoidal vector fields. Thus the velocity vector field $\langle \boldsymbol{u} \rangle$ can be expressed as

$$\langle \boldsymbol{u} \rangle = \langle \boldsymbol{u}_p \rangle + \langle \boldsymbol{u}_e \rangle, \tag{7}$$

where $\langle \boldsymbol{u}_p \rangle$ is an irrotational component, and $\langle \boldsymbol{u}_e \rangle$ is a solenoidal (rotational) component and $\langle \cdot \rangle$ is an operator to take an ensemble average. By definition,

$$\mathrm{rot}\,\langle \boldsymbol{u}_p \rangle = 0, \quad \mathrm{div}\,\langle \boldsymbol{u}_p \rangle = \langle \theta \rangle, \tag{8}$$

$$\mathrm{rot}\,\langle \boldsymbol{u}_e \rangle = \langle \zeta \rangle, \quad \mathrm{div}\,\langle \boldsymbol{u}_e \rangle = 0, \tag{9}$$

where $\langle \theta \rangle$ and $\langle \zeta \rangle$ are the source density and vorticity of $\langle \boldsymbol{u} \rangle$, respectively. The irrotational component $\langle \boldsymbol{u}_p \rangle$ has a velocity potential Φ, then

$$\langle \boldsymbol{u}_p \rangle = \mathrm{grad}\,\Phi. \tag{10}$$

In the surf zone, the source density $\langle \theta \rangle$ is substantially zero. Hence from (8) and (10) the velocity potential Φ satisfies the following Laplace equation:

$$\nabla^2 \Phi = 0. \tag{11}$$

To execute the separation as expressed in (7), we must evaluate the irrotational component $\langle \boldsymbol{u}_p \rangle$ from (11) and the observed data. For this purpose, we may use Dean's (1965) stream function method by which the velocity field described in terms of the stream function is calculated so as to satisfy the Laplace equation and minimize the error for the boundary conditions at the water surface. Unfortunately, this method cannot be utilized for breaking waves, in a strict sense at least, because of local breaking of the water surface. Hence, an alternative method, described as follows, has been developed.

The general solution of the Laplace equation (11) which satisfies the bottom boundary condition $\Phi_z = 0$ (at $z = -h$) for a horizontal bottom is

$$\Phi(x, z, t) = \int_{-\infty}^{\infty} A(k, t) \frac{\cosh k(z+h)}{\cosh kh} \mathrm{e}^{\mathrm{i}kx} \mathrm{d}k, \tag{12}$$

where k is a wavenumber, x and z are horizontal and vertical coordinates (z is measured upward from the mean water level) and t is time. The integration constant $A(k, t)$ in (12) is a time-varying wavenumber spectrum which may be determined, for non-breaking waves, from the remaining upper boundary conditions. For breaking waves, however, the upper boundary conditions cannot be used for the reason mentioned above; hence $A(k, t)$ should be evaluated by an alternative method. In the present method, $A(k, t)$ is estimated by the Fourier analysis of the velocity data measured at the level z_0 where the vorticity $\langle \zeta \rangle$ can be regarded practically as zero.

With a wavenumber–frequency spectrum $B(k, \omega)$, (12) can be expressed as

$$\Phi(x, z, t) = \int_{-\infty}^{\infty} \int_{0}^{\infty} B(k, \omega) \frac{\cosh k(z+h)}{\cosh kh} \mathrm{e}^{\mathrm{i}(kx+\omega t)} \mathrm{d}\omega\, \mathrm{d}k. \tag{13}$$

$B(k,\omega)$ may be assumed to have the form,

$$B(k,\omega) = E_1(\omega)\,\delta(k-k_1(\omega)) + E_2(\omega)\,\delta(k+k_2(\omega)), \tag{14}$$

in which $\delta(\cdot)$ is Dirac's delta function, $E_1(\omega)$ and $E_2(\omega)$ represent the frequency spectra of reflected and incident waves, respectively, and $k_1(\omega)$ and $k_2(\omega)$ indicate their dispersion relations. Substitution of (14) into (13) leads to

$$\Phi(x,z,t) = \int_0^\infty E_1(\omega)\frac{\cosh k_1(z+h)}{\cosh k_1 h}e^{i(k_1 x+\omega t)}d\omega + \int_0^\infty E_2(\omega)\frac{\cosh k_2(z+h)}{\cosh k_2 h}e^{i(-k_2 x+\omega t)}d\omega. \tag{15}$$

If E_{1_n}, E_{2_n}, k_{1_n}, k_{2_n} and $\omega_n (n = 0, 1, 2, \ldots, N)$ denote discrete forms of E_1, E_2, k_1, k_2 and ω, a finite Fourier power series approximation of (15) becomes

$$\Phi(x,z,t) = \sum_{n=0}^{N} E_{1_n}\frac{\cosh k_{1_n}(z+h)}{\cosh k_{1_n} h}e^{i(k_{1_n}x+\omega_n t)}\Delta\omega + \sum_{n=0}^{N} E_{2_n}\frac{\cosh k_{2_n}(z+h)}{\cosh k_{2_n} h}e^{i(k_{2_n}x+\omega_n t)}\Delta\omega. \tag{16}$$

The horizontal position x in the above equation may be regarded as zero, since in the present method the velocity field at a fixed value of x is of concern. Assuming $k_{1_n} = k_{2_n} = k_n$, we can obtain

$$\Phi = \sum_{n=0}^{N} (E_{1_n}+E_{2_n})\frac{\cosh k_n(z+h)}{\cosh k_n h}e^{i\omega_n t}\Delta\omega. \tag{17}$$

Horizontal and vertical components of $\langle \boldsymbol{u}_p \rangle$ are

$$\langle u_p \rangle = i\sum_{n=0}^{N} k_n(E_{1_n}-E_{2_n})\frac{\cosh k_n(z+h)}{\cosh k_n h}e^{i\omega_n t}\Delta\omega, \tag{18}$$

$$\langle w_p \rangle = \sum_{n=0}^{N} k_n(E_{1_n}+E_{2_n})\frac{\sinh k_n(z+h)}{\cosh k_n h}e^{i\omega_n t}\Delta\omega. \tag{19}$$

Defining

$$F_{xn} = ik_n(E_{1_n}-E_{2_n})\frac{\cosh k_n(z_0+h)}{\cosh k_n h}\Delta\omega, \tag{20}$$

$$F_{zn} = k_n(E_{1_n}+E_{2_n})\frac{\sinh k_n(z_0+h)}{\cosh k_n h}\Delta\omega, \tag{21}$$

we can obtain final expressions for $\langle u_p \rangle$ and $\langle w_p \rangle$ as follows:

$$\langle u_p \rangle = \sum_{n=0}^{N} F_{xn}\frac{\cosh k_n(z+h)}{\cosh k_n(z_0+h)}e^{i\omega_n t}, \tag{22}$$

$$\langle w_p \rangle = \sum_{n=0}^{N} F_{zn}\frac{\sinh k_n(z+h)}{\sinh k_n(z_0+h)}e^{i\omega_n t}. \tag{23}$$

F_{xn} and F_{zn} in the above equations can be estimated by a spectral analysis of velocity data at $z = z_0$. The nth wavenumber k_n may be evaluated from the celerity of the nth wave component which can be calculated, for example, by a cross-

spectrum of velocity data obtained simultaneously with two velocimeters aligned adequately in the x-direction. In the present paper, however, k_n is evaluated as $k_n = \omega_n/c$ for all n, in which c is the phase velocity of the wave as a whole, because only one velocimeter was available in the experiment. This assumes that the waves propagate without change of their shape and seems to contradict the deformable feature of the breaking waves. However Dean's stream function method, which requires the same assumption on the celerity, gives fairly good results even for the velocity field under deforming waves near the breaking point (Sakai & Iwagaki 1978; Hino & Kashiwayanagi, 1979; Nadaoka, Kondoh & Tanaka 1982). Hence, the permanent-shape assumption seems to produce no significant error in the estimation of the *local* velocity field by the present method.

The validity of the present method has been checked by applying it to an estimation of the irrotational velocity field of non-breaking waves. Though the results are not presented here (see Nadoaka 1986), comparison between the calculated and the measured velocity fields has shown sufficiently good agreement even for the case in which reflected waves are appreciably superimposed, while Dean's stream function theory has not yielded a good estimation because the theory is based on an assumption of progressive waves with permanent shape.

Although the present method is for a velocity field on a horizontal bottom, almost the same procedure can be applied to the case of an arbitrarily shaped bottom by using a conformal mapping technique derived by Nadaoka & Hino (1984). Further, the present method may be extended to extract turbulent components, which should be defined as vorticity-containing velocity fluctuations as mentioned in §4.2, by subtracting *instantaneous* irrotational velocity components from the raw data. This needs, however, a more elaborate experimental set-up and complicated data analysis.

5.2. *Vorticity effect on mass transport*

The velocity data described in the preceding section have been separated by the present method. The phase-averaged velocity data $\langle \boldsymbol{u} \rangle$ and their vorticity $\langle \zeta \rangle$ have already been given in figures 13 and 19, respectively. Figure 19 indicates that the vorticity $\langle \zeta \rangle$ in the zone $\tilde{z} = 4$–6 cm is practically zero; hence we can choose $z_0 = -9.82$ cm ($\tilde{z} = 5$ cm) in (22) and (23) where the velocity field consists almost entirely of the irrotational component.

The separated velocity fields, $\langle \boldsymbol{u}_p \rangle$ and $\langle \boldsymbol{u}_e \rangle$, are shown in figure 20(a, b). In this case, a uniform and offshoreward-directed velocity $-U_0$ is added to the irrotational component $\langle \boldsymbol{u}_p \rangle$ so that the mass flux through the entire water depth averaged over a wave period, $\overline{\int \langle u_p \rangle \, dz}$, becomes zero. Since the experiments were performed within a closed wave channel, the time-averaged total mass flux $\overline{\int \langle u \rangle \, dz}$ must be identically zero. Consequently, the time-averaged mass flux of the rotational component $\overline{\int \langle u_e \rangle \, dz}$ also becomes zero, resulting in offshoreward return flow in the region close to the bottom as shown in figure 20(b).

One of the remarkable features of the rotational flow field $\langle \boldsymbol{u}_e \rangle$ is the existence of a large amount of onshoreward flow beneath the wave crest, where the magnitude of $\langle \boldsymbol{u}_e \rangle$ is comparable with that of the irrotational velocity component $\langle \boldsymbol{u}_p \rangle$. The onshoreward flow still exists even in the wave trough region, though its magnitude is small. This means that in the upper layer of the water there exists substantial transport of fluid mass toward the shore.

As already shown in §3, breaking waves are characterized by the existence of an eddying structure in the region of the wave crest. The large-scale eddies with a large amount of vorticity area advected and diffused into the otherwise

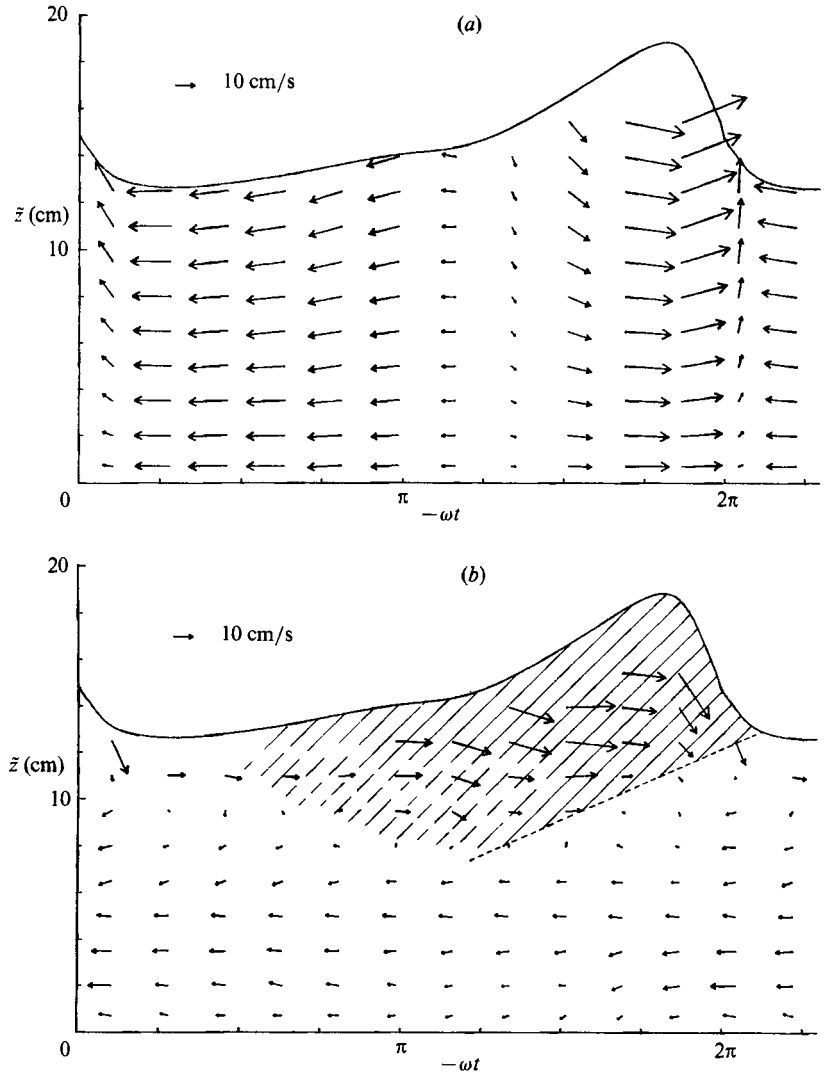

FIGURE 20. Separated velocity components: (*a*) irrotational velocity component, $\langle \boldsymbol{u}_p \rangle$; (*b*) rotational velocity component, $\langle \boldsymbol{u}_e \rangle$.

almost irrotational flow field. The hatched area in figure 20(*b*) represents the region in which the video images show the existence of large-scale eddies containing a noticeable amount of air bubbles. The figure indicates that the hatched area almost coincides with the region where the onshoreward rotational velocity component exists with an appreciable magnitude; this fact suggests that the large-scale eddies act to considerably increase the onshoreward mass flux beneath the wave crest.

Essentially, vortical fluid motion contrasts strongly with orbital wave motion in the sense that the former has an intrinsic property to transport fluid particles with it, whereas the latter is basically an oscillatory fluctuating motion even if mass transport of the second order of magnitude arises, referred to as the 'Stokes drift'. Hence, the large-scale eddy motion is responsible for the generation of the excessive mass flux as one of the most important effects of vorticity on the breaking waves. This remarkable effect of vorticity on the mass transport, as compared with the

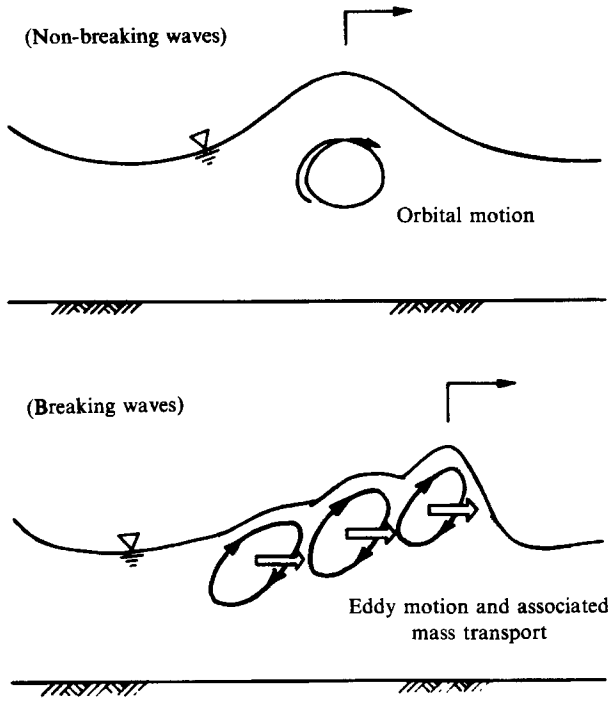

FIGURE 21. Conceptual illustration of the vorticity effects on mass transport.

orbital motion under normal waves, is illustrated conceptually in figure 21. Emphasis should be placed on the difference between the present description of mass transport, where several vortices generated in sequence migrate to the shore with a speed less than the bore propagation velocity c (cf. figures 5 and 6), and that of Svendsen (1984*a*, *b*) in which the single roller attached to a bore front conveys the water mass in the roller with a speed c.

Nadaoka & Kondoh (1982) pointed out that the mean mass flux toward the shore is enhanced within the highly turbulent flow region of the surf zone as compared with that calculated as normal non-breaking wave motion by Dean's stream function method, while the measured flux shows nearly the same value as that calculated around and outside the breaking point. This is attributable to the vorticity effect on the mass transport described above.

5.3. *Vorticity effects on momentum transport*

Figure 22 shows the distribution of $-\langle uw\rangle$, the phase average of $-uw$, which has a noticeably large positive peak at the wave crest as well as a negative peak beneath the wave front. Comparing this figure with figures 15 and 16 we can see that the Reynolds stress $-\langle u'w'\rangle$ is responsible for the appearance of the second positive peak at $\tilde{z} \approx 12.5$ cm just behind the wave crest.

To examine the vorticity effects on the momentum transport, $-\langle uw\rangle$, the difference between $-\langle uw\rangle$ and $-\langle u_{\mathrm{p}} w_{\mathrm{p}}\rangle$ was calculated. As shown in figure 23, the negative values in the region beneath the wave front no longer exist. Therefore, the negative values of $-\langle uw\rangle$ beneath the wave front are considered to be due to the velocity fluctuation as 'wave' motion.

In figure 23 the region where $-\langle uw\rangle + \langle u_{\mathrm{p}} w_{\mathrm{p}}\rangle$ takes positive large values almost

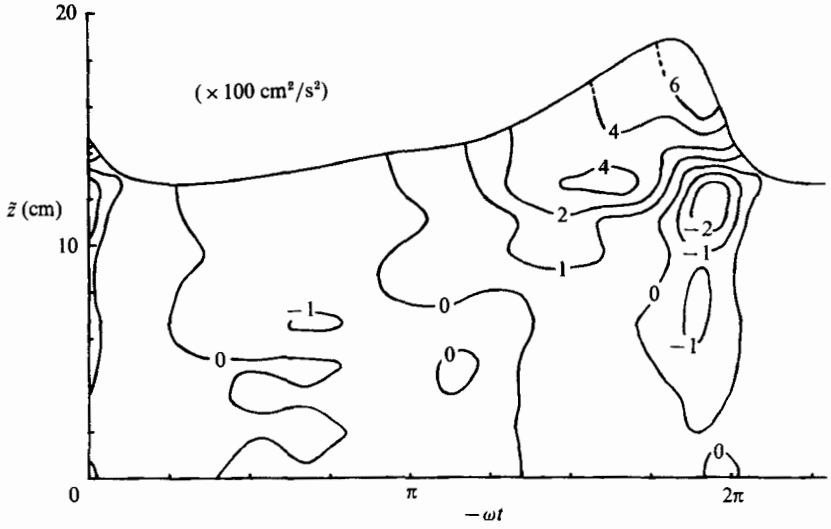

FIGURE 22. Phase-averaged momentum transport, $-\langle uw \rangle$.

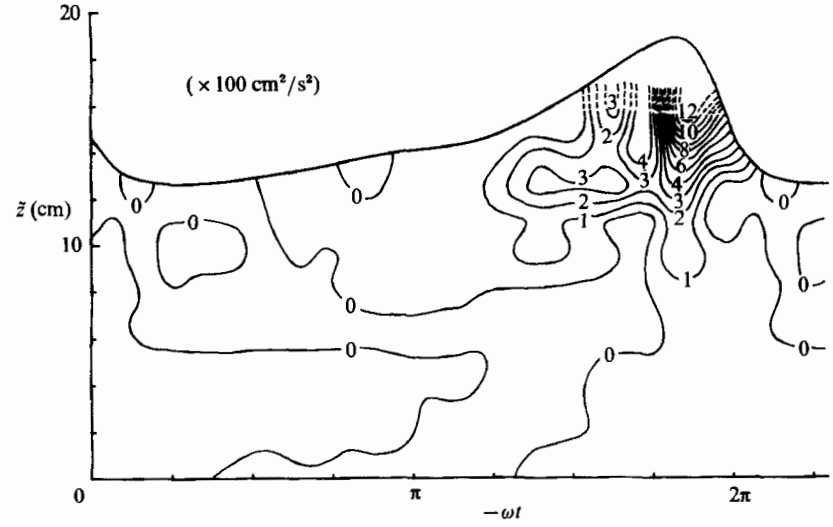

FIGURE 23. Difference between $-\langle uw \rangle$ and $-\langle u_p w_p \rangle$.

corresponds to the large-scale eddy region. Furthermore, their absolute values are larger than those for the negative values due to the irrotational velocity component shown in figure 22. These facts emphasize that the rotational velocity component produced by wave breaking plays an important role not only in the mass transport but also in the momentum transport process.

5.4. *Vorticity effects on water surface elevation*

5.4.1. *Inverse estimation method for water surface elevation*

For non-breaking waves, the water surface elevation η and the time-varying wavenumber spectrum $A(k, t)$ in (12) can be determined so as to satisfy the kinematic and the dynamic boundary conditions on the water surface η. If one of these

unknown variables η and A is evaluated, another variable may be estimated from one or both of the water surface boundary conditions. In the usual methods, the water surface elevation η is given from measurements, and then the associated spectrum $A(k,t)$ or velocity field $\boldsymbol{u}$ is to be estimated. The linear filter method (Reid 1957) and the extended velocity potential method (Lambrakos 1981) as well as the stream function method (Dean 1965) fall into this category.

In the present case, on the other hand, the velocity field $\boldsymbol{u}$ has been calculated through (22) and (23) based on a spectral analysis of the measured velocity data at a specified location. Hence the water surface elevation η which is consistent with the irrotational velocity field may be calculated from the water surface boundary conditions. Denoting the water surface elevation to be estimated as $\hat{\eta}$ and using (22) and (23), the time derivative of Φ and the irrotational velocity components at the water surface are expressed as follows:

$$\Phi_t|_{z=\hat{\eta}} = \mathrm{Re}\left\{ \sum_{n=0}^{N} \mathrm{i}\omega_n F_{zn} \frac{1}{k_n \tanh k_n(z_0+h)} \frac{\cosh k_n(\hat{\eta}+h)}{\cosh k_n(z_0+h)} \mathrm{e}^{\mathrm{i}\omega_n t} \right\}, \tag{24}$$

$$u_{\mathrm{p}}|_{z=\hat{\eta}} = \mathrm{Re}\left\{ \sum_{n=0}^{N} F_{xn} \frac{\cosh k_n(\hat{\eta}+h)}{\cosh k_n(z_0+h)} \mathrm{e}^{\mathrm{i}\omega_n t} - U_0 \right\}, \tag{25}$$

$$w_{\mathrm{p}}|_{z=\hat{\eta}} = \mathrm{Re}\left\{ \sum_{n=0}^{N} F_{zn} \frac{\sinh k_n(\hat{\eta}+h)}{\sinh k_n(z_0+h)} \mathrm{e}^{\mathrm{i}\omega_n t} \right\}. \tag{26}$$

In the above equations, the ensemble-mean symbol $\langle \cdot \rangle$ is dropped for the sake of simplicity of the notation. Since the estimation of $\hat{\eta}_x$ in the kinematic boundary condition is difficult when reflected waves of perceptible magnitude are superimposed when only one wave gauge is available, only the following dynamic boundary condition is used in the present procedure:

$$\Phi_t + \tfrac{1}{2}(u_{\mathrm{p}}^2 + w_{\mathrm{p}}^2) + g\hat{\eta} = \text{const.} \quad \text{at } z = \hat{\eta}. \tag{27}$$

For $\hat{\eta}$, an additional condition,

$$\int_0^T \hat{\eta}\, \mathrm{d}t = 0. \tag{28}$$

must be satisfied.

From these equations, the wave profile $\hat{\eta}$ has been determined by the following iteration procedure. First the Bernoulli constant in (27) at an arbitrary phase, for example at the zero-up crossing point of the measured wave profile, is estimated by assuming a value of $\hat{\eta}$ at that phase. Then, (27) for the same Bernoulli constant, together with (24)–(26), yields the values of $\hat{\eta}$ at all other phases with an iterative procedure. If the wave profile $\hat{\eta}$ so obtained does not satisfy the condition (28), the assumed value of $\hat{\eta}$ at the initial phase should be modified and the calculation should be continued until the integrated value of $\hat{\eta}$ with respect to t becomes sufficiently small. The resultant values of $\hat{\eta}$ are taken as the estimated values of $\hat{\eta}$.

The present method has been confirmed, for non-breaking waves, to give a good estimation of water surface profiles in satisfactory agreement with measured profiles (see e.g. Nadaoka 1986).

5.4.2. *Wave profile consistent with the irrotational velocity field of breaking waves*

For breaking waves, the dynamic boundary condition of (27) need not be satisfied because of the occurrence of the rotational velocity component due to the wave breaking at the water surface. Hence, in general, the wave profile estimated by the

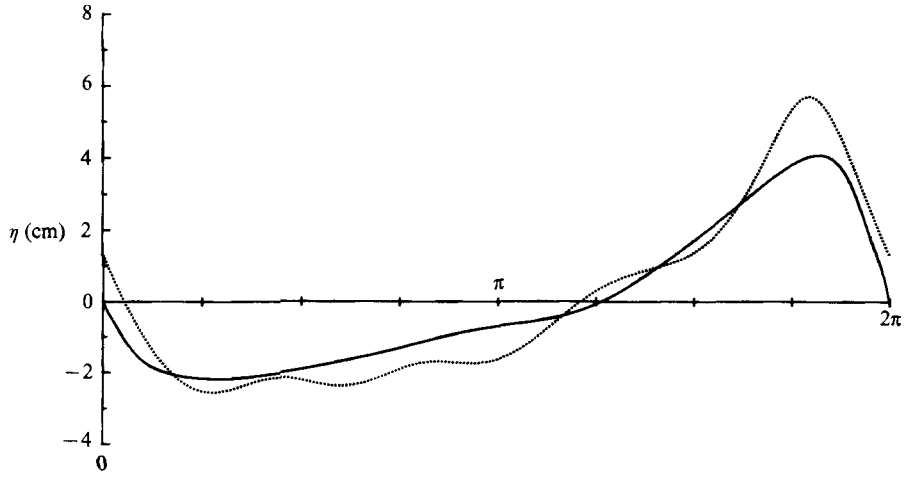

FIGURE 24. Inversely estimated wave profile consistent with ·····, the irrotational velocity field; and ——, measured wave profile.

above method may be different from the measured wave profile. Conversely, however, the occurrence of such a difference allows us to obtain valuable information on the role of the rotational velocity component in the wave dynamics.

The wave profile estimated from the procedure described, figure 24, shows that, at the wave crest, the measured water surface elevation becomes smaller than the estimated water surface elevation $\hat{\eta}$. This means that the potential energy of the waves is converted into kinetic energy, yielding excessive mass flux in the direction of wave propagation at the water surface and thus diminishing the wave height. This reflects the effect of vorticity on the mass flux described in §5.2, demonstrating another aspect of the importance of vorticity effects on breaking wave dynamics.

6. Conclusions

To examine the structure of turbulence and its role in breaking wave dynamics, laboratory experiments were extensively carried out in which Eulerian velocity measurements using a fibre-optic LDV and several flow visualizations had been made. Close analyses of the experimental results clearly show that one of the most significant features of wave breaking, and the resultant occurrence of intensive turbulence, is to generate a large amount of vorticity associated with the large-scale eddies. This strongly affects the breaking wave dynamics through the considerable increase in mass and momentum transport and thus a decrease in wave height.

The results and conclusions obtained can be summarized as follows.

(i) Flow visualizations and Eulerian velocity measurements demonstrate that there exists a characteristic large-scale eddy structure under breaking waves, i.e. dominant eddies around the wave crest have a rather two-dimensional flow structure with its axis parallel to the crest line (horizontal eddies), while behind the wave crest, the eddy structure changes quickly into that of obliquely downward stretched eddies with strong three-dimensionality (obliquely descending eddies).

(ii) Simultaneous velocity measurements with flow visualization have revealed that these large-scale eddies are mainly responsible for the generation of Reynolds stress in the upper layer of the water.

(iii) As a result, the large-scale eddies also affect the deformation characteristics

of the mean flow field such as the mean strain rate and principal direction. A considerable amount of vorticity is generated at the front face of the breaking waves and entrained, by the large-scale eddies, into the underlying flow field.

(iv) The most significant property of the velocity field within the surf zone is that an irrotational velocity component, as 'wave motion', coexists with a rotational mean velocity component, as 'eddying motion', with non-zero mean vorticity generated through the wave breaking process.

Through separation of a phase-averaged velocity field into irrotational and rotational components, several effects on the breaking wave dynamics of the mean vorticity associated with the large-scale eddies have been examined. The separated components of a velocity field show that the generation of the vorticity-containing mean velocity component causes considerable increase in mass and momentum transport. Furthermore, by inversely estimating the water surface profile corresponding to the separated irrotational mean velocity field, it is found that the vorticity effects also have fundamental significance for the dynamics governing the water surface elevation of breaking waves.

REFERENCES

BATTJES, J. A. & SAKAI, T. 1980 Velocity field in a steady breaker. *J. Fluid Mech.* **111**, 421–437.

DEAN, R. G. 1965 Stream function representation of nonlinear ocean waves. *J. Geophys. Res.* **70**, 4561–4572.

HATTORI, M. & AONO, T. 1985 Experimental study on turbulence structures under breaking waves. *Coastal Engng Japan* **28**, 97–116.

HINO, M. & KASHIWAYANAGI, M. 1979 Applicability of Dean's stream function method to estimation of orbital wave velocity and wave set-down and set-up. *Coastal Engng Japan* **22**, 11–20.

HINO, M., SAWAMOTO, M., YAMASHITA, T., HIRONAGA, M. & MURAMOTO, T. 1984 *Prototype 2-dimensional LDV Adopting Optical Fibres, Laser-Doppler Velocimetry and Hot-Wire/Film Anemometry*, pp. 97–105. Association for the Study of Flow Measurement, Osaka, Japan.

LAMBRAKOS, K. F. 1981 Extended velocity potential wave kinematics. *J. Waterways Port Coastal Ocean Div. ASCE* **107**, (WW3) 159–174.

MILLER, R. L. 1976 Role of vortices in the surf zone prediction: sedimentation and wave forces. *Beach and Nearshore Sedimentation, SEPM Spec. Pub.* 23, pp. 92–114.

NADAOKA, K. 1986 A fundamental study on shoaling and velocity field structure of water waves in the nearshore zone. Doctoral Dissertation, Tokyo Inst. of Tech. (reproduced in *Tech. Rep. of Dept. Civil Engng, Tokyo Inst. Tech.*, No. 36, pp. 33–125, 1986.)

NADAOKA, K. & HINO, M. 1984 Conformal mapping solution of a wave field on the arbitrarily shaped sea bed. *Proc. 19th Conf. on Coastal Engng*, pp. 1192–1208. ASCE.

NADAOKA, K. & KONDOH, T. 1982 Laboratory measurements of velocity field structure in the surf zone by LDV. *Coastal Engng Japan* **25**, 125–145.

NADAOKA, K., KONDOH, T. & TANAKA, N. 1982 The structure of velocity field within the surf zone revealed by means of laser-Doppler anemometry. *Rep. Port and Harbour Res. Inst.*, Vol. 21, No. 2, pp. 49–106 (in Japanese).

PEREGRINE, D. H. 1983 Breaking waves on beaches, *Ann. Rev. Fluid Mech.* **15**, 149–178.

PEREGRINE, D. H. & SVENDSEN, I. A. 1978 Spilling breakers, bores and hydraulic jumps. *Proc. 16th Conf. on Coastal Engng*, pp. 540–550. ASCE.

REID, R. O. 1957 Correlation of water level variation of non-linear ocean waves. *Proc. 6th Coastal Engng*, pp. 749–786. ASCE.

SAKAI, T., INADA, Y. & SANDANBATA, I. 1982 Turbulence generated by wave breaking on beach. *Proc. 18th Conf. on Coastal Engng*, pp. 3–21. ASCE.

SAKAI, T. & IWAGAKI, Y. 1978 Estimation of water particle velocity of breaking waves. *Proc. 16th Conf. on Coastal Engng*, pp. 551–568. ASCE.

SAKAI, T., SANDANBATA, I. & UCHIDA, M. 1984 Reynolds stress in surf zone. *Proc. 19th Conf. on Coastal Engng*, pp. 42–53. ASCE.

STIVE, M. J. F. 1980 Velocity and pressure field of spilling breakers. *Proc. 17th Conf. on Coastal Engng*, pp. 547–566. ASCE.

STIVE, M. J. F. & WIND, H. G. 1982 A study of radiation stress and set-up in the nearshore region. *Coastal Engng* **6**, 1–26.

SVENDSEN, I. A. 1984*a* Wave hights and set-up in a surf zone. *Coastal Engng* **8**, 303–329.

SVENDSEN, I. A. 1984*b* Mass flux and undertow in a surf zone. *Coastal Engng* **8**, 347–365.

TENNEKES, H. & LUMLEY, J. L. 1972 *A First Course in Turbulence*. MIT Press.